Genesis of Electric Field assisted Microparticle Assemblage in a Dielectric Fluid

Satarupa Dutta[1], Amit Kumar Singh[2], Partho Sarathi Gooh Pattader[1,2], and Dipankar Bandyopadhyay[1,2]†

[1]Department of Chemical Engineering, Indian Institute of Technology Guwahati, Assam 781039, India

[2]Centre for Nanotechnology, Indian Institute of Technology Guwahati, Assam 781039, India

(Received xx; revised xx; accepted xx)

1. Supplementary Information

1.1. *Validation of Numerical Method*

For the purpose of validation of the numerical method mentioned in section 3 of the main manuscript the normalized electrical force ${F_e}^*\left(=\frac{F_e}{qE_0}\right)$ experienced by a conductive particle ($r_s = 0.5$ mm) oscillating between parallel electrodes 20 mm apart obtained numerically is compared to the force obtained analytically by **?**. If h is defined as the distance between the centre of the particle and the grounded electrode at $z = 0$, and d as the distance between the electrodes, then the analytical expressions for the force experienced by the particles read as (**??**) as,

$$F_e = 4\pi\varepsilon_f {r_s}^2 {E_0}^2 F_0\left(\frac{h}{r_s}\right) + qE_0F_1\left(\frac{h}{r_s}\right) + \frac{q^2}{4\pi\varepsilon_f {r_s}^2}F_2\left(\frac{h}{r_s}\right), \qquad h \leqslant \frac{d}{2} \quad (1.1)$$

$$F_e = -4\pi\varepsilon_f {r_s}^2 {E_0}^2 F_0\left(d-h\right) + qE_0F_1\left(d-h\right) - \frac{q^2}{4\pi\varepsilon_f {r_s}^2}F_2\left(d-h\right), \qquad h > \frac{d}{2} \quad (1.2)$$

where, E_0 is the average electric field intensity between the electrodes in absence of the solid particle. The coefficients F_0, F_1 and F_2 are defined elsewhere (**?**). Figure 1(a) shows the variation of ${F_e}^*$ with the normalized distance $h^*\left(=\frac{h-r_s}{r_s}\right)$ obtained numerically alongside the corresponding values obtained from equations (1.1) and (1.2). It can be seen from the figure that when the particle is sufficiently close to either electrode, the force predicted numerically (solid symbols) is marginally different from the corresponding values predicted analytically (hollow symbols), with a maximum relative error $\left(\left|\frac{{F_{e,}}^*{}_{numerical} - {F_{e,}}^*{}_{analytical}}{{F_{e,}}^*{}_{numerical}}\right| \times 100\%\right)$ of $\sim 3.8\%$. It may be hypothesized that presence of the particle between parallel electrodes, as considered in the numerical solution, leads to the influence of the image charges on the total force experienced by the particle, which leads to the deviation from the analytically obtained values. Figure 1(b) predicts the comparison of the variation of dimensionless drag coefficient (λ_d) with the dimensionless position (h/r_s) of the particle between two electrodes obtained by

† Email address for correspondence: dipban@iitg.ac.in

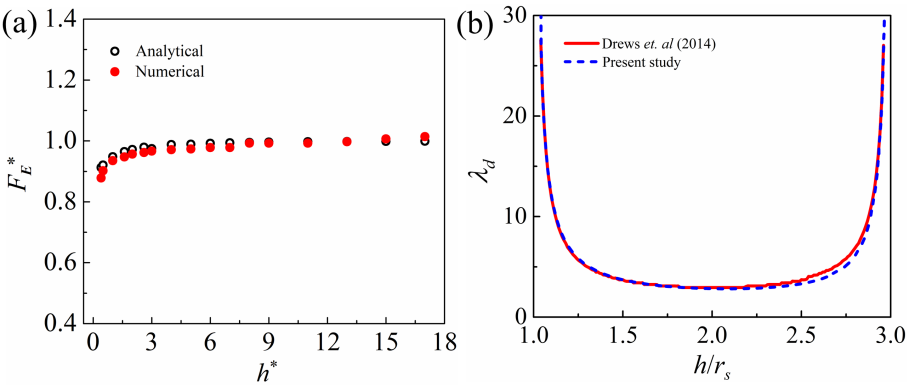

FIGURE 1. (*a*) Variation of normalized electric force (F_e^*) acting on a solid particle with its normalized distance (h^*) from the grounded bottom electrode. The solid (hollow) symbols denote the numerically (analytically) obtained values, respectively. The other parameters used for the numerical simulations are: $r_s = 0.5$ mm, $d = 20$ mm, $\varepsilon_f = 2.5\varepsilon_0$, $q = 7 \times 10^{-11}$ C and $E_0 = 6$ kVcm^{-1}. (*b*) Variation of drag coefficient (λ_d) with normalized distance (h/r_s) of the particle from the grounded electrode at $z = 0$. The dashed (solid) line denotes values obtained numerically (analytically obtained by **?**) from the present study, respectively, for an aspect ratio (d/r_s) of 4.

the present numerical method to that reported analytically by **?**. The drag coefficient captures the increase in the drag force experienced by the particle due to the presence of the walls and can be calculated from the following equation,

$$\lambda_d = \frac{\boldsymbol{F}_e}{6\pi\mu_f r_s \boldsymbol{v}_s}. \tag{1.3}$$

It must be noted that equation (1.3) is valid when inertial acceleration of the particle is small compared to drag forces (**?**). The plots in figure 1(*b*) suggests a reasonable agreement of the values of drag coefficient obtained numerically and analytically. Both the plots suggest significant increase in the drag coefficient close to the walls due to increase in the hydrodynamic drag force experienced by the particle.

1.2. *Grid Convergence Study*

To ensure the grid independence of the numerical simulation results, a grid convergence study was carried out by considering four grid resolutions (G_R) tabulated in figure 2(*a*). For the purpose of the test, two equal sized spheres 1 and 2 were subjected to an electric field of magnitude 9 kVcm^{-1}. The spheres were assigned the theoretical values of charge of opposite polarity (sphere 1 positively charged and sphere 2 negatively charged). At time $t = 0$, the positions of the spheres 1 and 2 were $h = 3.8$ mm and $h = 1.3$ mm, respectively. On application of electric field the spheres were subjected to electric force and the values of the z-component of the Maxwell stress tensor at the bottommost point of sphere 1 ($\tau_z{}^b$) and the topmost point of sphere 2 ($\tau_z{}^t$) are tabulated in figure 2(*a*) and shown in figure 2(*b*), for four different grid resolutions. Both figures (*a*) and (*b*) suggest that the convergence improves with grid refinement. Table 2(*a*) predicts that the relative errors in the values of $\tau_z{}^t$ and $\tau_z{}^b$ for grid resolutions C (46546 elements) and D (56681 elements), are $\sim$0.1%. Hence, grid C was chosen for the numerical simulations to optimize the computational load.

(a)

G_R	No. of elements	$\tau_z{}^t$	Error (%)	$\tau_z{}^b$	Error (%)
A	15797	183.88846	--	-183.55259	--
B	32281	185.74894	1.0117	-185.57618	1.1024
C	46546	186.1287	0.2044	-185.99532	0.226
D	56681	186.32837	0.107	-186.19953	0.109

(b)

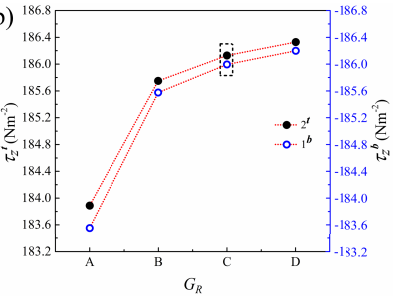

FIGURE 2. (*a*) Tabulated values of the number of mesh elements corresponding to each grid resolution (G_R), the values of the z- component of the Maxwell stress tensor at the bottommost point of sphere 1 ($\tau_z{}^b$) and the topmost point of sphere 2 ($\tau_z{}^t$) at $t = 0.06$ s and the relative error for the mentioned grid resolutions. (*b*) Variation of $\tau_z{}^t$ and $\tau_z{}^b$ with the grid resolutions. The rectangular box at C represents the chosen grid resolution for the numerical simulations. The other parameters for the simulations are, $E_0 = 9$ kVcm^{-1}, $r_s = 0.5$ mm for each sphere (1 and 2), $d = 5$ mm, $\mu_f = 0.3$ Pa.s, $\varepsilon_f = 2.5\varepsilon_0$, $\rho_f = 970$ kgm^{-3} and $\rho_s = 1280$ kgm^{-3}.

1.3. *Characterization of the Beads*

1.3.1. *Materials*

Iron (II) sulphate heptahydrate ($FeSO_4.7H_2O$), hydrochloric acid (HCl) (37%), ethanol (C_2H_5OH) (99.9%), and Amberlite IR-120 particles were obtained from Merck (India). Iron (III) chloride hexahydrate ($FeCl_36H_2O$), silver nitrate ($AgNO_3$), Nickel (II) chloride hexahydrate ($NiCl_2.\ 6H_2O$), and sodium borohydride ($NaBH_4$) were procured from Sigma-Aldrich (India). The aforementioned chemicals were used without further purification. The Milli-Q grade water was used in the experiments.

1.3.2. *Methods*

The deposition of metallic entities on the ion-exchange Amberlite IR-120 resin particles was performed by following the previously reported protocols with slight modifications (**???**). Initially, 3 g of Amberlite IR-120 (cationic exchange resin particles) were thoroughly washed with MilliQ grade water and then immersed in 20 ml of HCl (0.3 M) and kept for 8 h at 25°C for activation. After activation, the particles were washed with water to remove the excess HCl and then dried overnight at 60°C. Thereafter, the particles were suspended overnight in a beaker containing 20 ml of 1.5 M of metal salt solution ($FeSO_4.7H_2O$, $NiCl_2.6H_2O$, $AgNO_3$) at 25°C. In case of $AgNO_3$ treatment, the beaker was completely covered with aluminium foil and was kept in dark conditions in order to prevent or slow down the light-mediated decomposition of the silver salt. The higher concentration of metallic salt solution was used in this protocol to ensure formation of densely-packed nanoparticle (NP) aggregates or metallic thin films over the resin particles rather than discrete metallic NPs, after reduction process. Following this, the particles were retrieved after metal salt treatment and then suspended in a beaker containing 5 ml of water. After this, 10 ml of $NaBH_4$ (0.8 M) was added dropwise to the suspension with vigorous stirring. The black colouration of the particles indicated the formation of iron (Fe) and nickel (Ni) coating on the polymer particles and in the case of silver (Ag) coating, a metallic silvery appearance was observed on the spherical particles. The particles were washed thrice with ethanol to prevent rapid oxidation, and vacuum dried for 1 h at 60°C. The freshly prepared metal-coated particles were used for all the experiments. The uncoated and freshly prepared metal-coated Amberlite IR-120 resin particles were characterized using Field emission scanning electron microscopy

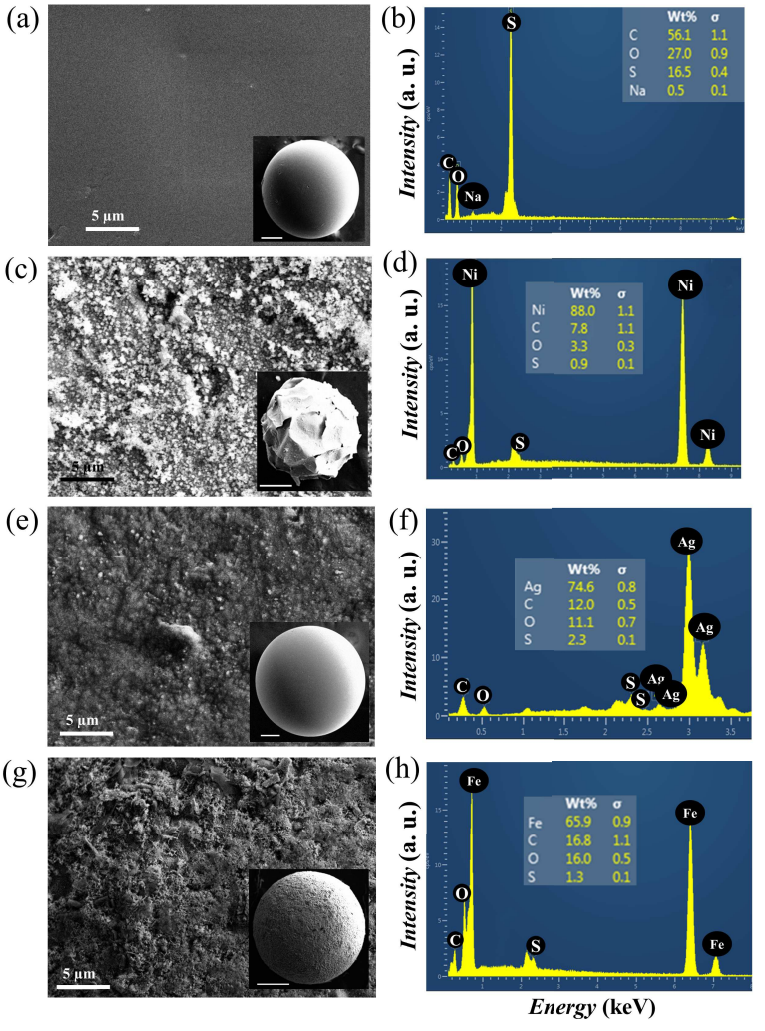

FIGURE 3. (*a*) Field Emission Scanning Electron Microscopy (FESEM) image of the surface of an uncoated Amberlite IR-120 polymer resin particle. The scale bar at the bottom is of 5 µm. The inset image shows an uncoated spherical resin particle. The scale bar at the bottom is of 125 µm. (*b*) Spot Energy Dispersive X-ray (EDX) of the uncoated polymer resin. (*c*) FESEM image of the surface of a freshly prepared nickel (Ni)-coated resin particle. The scale bar at the bottom is of 5 µm. The inset image shows a spherical Ni-coated resin particle. The scale bar at the bottom is of 250 µm. (*d*) Spot EDX of spherical Ni-coated resin particle shows the elemental Ni peak. (*e*) FESEM image of the surface of a freshly prepared silver (Ag)-coated resin particle. The scale bar at the bottom is of 5 µm. The inset image shows a spherical Ag-coated resin particle. The scale bar at the bottom is of 125 µm. (*f*) Spot EDX of spherical Ag-coated resin particle shows the elemental Ag peak. (*g*) FESEM image of the surface of a freshly prepared iron (Fe)-coated resin particle. The scale bar at the bottom is of 25 µm. The inset image shows a spherical Fe-coated resin particle. The scale bar at the bottom is of 250 µm. (*h*) Spot EDX of spherical Fe-coated resin particle shows the elemental Fe peak.

(Zeiss Sigma FESEM, Germany). The FESEM images shown in figure 3(*c*), figure 3(*e*) and figure 3(*g*) of an Amberlite IR-120 resin surface shows the presence of a homogenous thin film or coating of Ni, Ag and Fe, respectively, resulting in rough surface texture as compared to the uncoated resin (figure 3(*a*)). The spot EDX analysis - figure 3(*d*), figure

3(f) and figure 3(h) on the agglomerates confirmed the presence of the elemental Ni, Ag and Fe deposits, respectively, over the surface of the resin particles.

1.4. *Experimental Determination of Charge Acquired by the Particle*

In order to estimate the total charge acquired by the particle (q) in contact with the electrode, the following force balance, neglecting the acceleration of the particles, is used (**??**),

$$qE_0 = 6\pi\mu_f r_s v_s \lambda_d. \tag{1.4}$$

The average electric field intensity is calculated as, $E_0 = \dfrac{\psi_0}{d}$, where ψ_0 is the applied potential and d is the distance between the electrodes. The term on the left-hand side of the equation is the Coulomb force acting on the charged droplet. The term on the R.H.S. of equation 1.4 accounts for the drag force experienced by the particle. The dimensionless drag coefficient (λ_d) is obtained from figure 4(b). The frames extracted from the recorded videos are used to estimate the average speed (v_s) of the particles. Particle motions near the electrodes are not taken in the calculations.

REFERENCES

Dey, K. K., Sharma, D., Basu, S. & Chattopadhyay, A. 2008 Veering the motion of a magnetic chemical locomotive in a liquid. *J. Chem. Phys.* **129** (12), 121101.

Drews, A. M., Cartier, C. A. & Bishop, K. J. M. 2015 Contact charge electrophoresis: Experiment and theory. *Langmuir* **31** (13), 3808–3814.

Drews, A. M., Kowalik, M. & Bishop, K. J. M. 2014 Charge and force on a conductive sphere between two parallel electrodes: A stokesian dynamics approach. *J. Appl. Phys.* **116** (7), 074903.

Eslami, G., Esmaeilzadeh, E. & Pérez, A. T. 2016 Modeling of conductive particle motion in viscous medium affected by an electric field considering particle-electrode interactions and microdischarge phenomenon. *Phys. Fluids* **28** (10), 107102.

Im, D. J., Ahn, M. M., Yoo, B. S., Moon, D., Lee, D. W. & Kang, I. S. 2012 Discrete electrostatic charge transfer by the electrophoresis of a charged droplet in a dielectric liquid. *Langmuir* **28** (32), 11656–11661.

Pérez, A. T. 2002 Charge and force on a conducting sphere between two parallel electrodes. *J. Electrostat.* **56** (2), 199–217.

Singh, A. K., Dey, K. K., Chattopadhyay, A., Mandal, T. K. & Bandyopadhyay, D. 2014 Multimodal chemo-magnetic control of self-propelling microbots. *Nanoscale* **6** (3), 1398–1405.

Singh, A. K., Rarotra, S., Pasumarthi, V., Mandal, T. K. & Bandyopadhyay, D. 2018 Formic acid powered reusable autonomous ferrobots for efficient hydrogen generation under ambient conditions. *J. Mater. Chem. A* **6** (19), 9209–9219.